

Revision 1

A first-principles study of water in wadsleyite and ringwoodite: Implication for the 520-km discontinuity

Wenzhong Wang^{a, b, c, *}, Zhongqing Wu^{a, d, e}

^aLaboratory of Seismology and Physics of Earth's Interior, School of Earth and Space Sciences, University of Science and Technology of China, Hefei, Anhui 230026, China

^bDepartment of Earth Sciences, University College London, London WC1E 6BT, United Kingdom

^cEarth and Planets Laboratory, Carnegie Institution for Science, Washington, DC 20015, USA

^dNational Geophysical Observatory at Mengcheng, University of Science and Technology of China, Hefei, China

^eCAS Center for Excellence in Comparative Planetology, USTC, Hefei, Anhui 230026, China

*Correspondence to: Wenzhong Wang (wz30304@mail.ustc.edu.cn or wenzhong.wang@ucl.ac.uk)

1 **Abstract**

2 The seismic discontinuity around 520 km is believed to be caused by the phase
3 transition from wadsleyite to ringwoodite, the dominant minerals in the mantle
4 transition zone (MTZ). Both wadsleyite and ringwoodite can contain more than one
5 weight percentage of water at MTZ's conditions, but it is not well known how water
6 affects the wadsleyite-ringwoodite transition. Here we investigated water partitioning
7 between wadsleyite and ringwoodite and the water effect on this phase boundary using
8 first-principles calculations. Our results show that the presence of water will shift the
9 phase boundary to higher pressures and the width of the two-phase coexistence domain
10 in the $\text{Mg}_2\text{SiO}_4\text{-H}_2\text{O}$ system is insignificant at mid-MTZ conditions. For the
11 $(\text{Mg}_{0.9}\text{Fe}_{0.1})_2\text{SiO}_4$ system, the incorporation of 1.0 wt% water can narrow the effective
12 width of two-phase coexistence by two-thirds. Together with elastic data, we find that
13 that velocity and impedance contrasts are only mildly changed by the water partitioning.
14 We suggest that compared to the anhydrous condition, the presence of 1.0 wt% water
15 will increase velocity gradients across the wadsleyite-ringwoodite transition by
16 threefold, enhancing the detectability of the 520-km discontinuity.

17 **Keywords:** water partitioning, wadsleyite, ringwoodite, 520-km discontinuity, two-
18 phase coexistence, mantle transition zone

19

20 **1. Introduction**

21 Seismological studies have provided some of the most direct observations on the
22 Earth's mantle (Dziewonski and Anderson 1981; Kennett et al. 1995; Shearer and
23 Flanagan 1999) and understanding its physical and chemical properties
24 requires detailed knowledge from mineral physics. Olivine is the most
25 abundant mineral in the Earth's upper mantle and its volume percentage is ~60% in the
26 widely accepted pyrolitic mantle composition (Ringwood 1962; Zou et al. 2018; Duan
27 et al. 2019). The 410-km and 660-km discontinuities, which separate the upper mantle
28 from the lower mantle, caused by the olivine-wadsleyite and post-spinel phase

29 transitions (Bina and Helffrich 1994; Helffrich and Wood 2001; Higo et al. 2001; Hirose
30 2002; Fei et al. 2004; Katsura et al. 2004), respectively. In the mid mantle transition
31 zone (MTZ), wadsleyite is expected to undergo a phase transition to ringwoodite
32 (Akaogi et al. 1989; Katsura and Ito 1989; Inoue et al. 2006; Yu et al. 2008; Tsujino et
33 al. 2019), and some seismic studies have observed a seismic discontinuity around 520
34 km depth in some regions such as Northeastern China and central Asia (Shearer 1990;
35 Gossler and Kind 1996; Deuss and Woodhouse 2001; Tian et al. 2016). However, unlike
36 the 410-km and 660-km discontinuities, the 520-km discontinuity is not ubiquitously
37 observed and absent in other regions such as the northeastern Pacific Ocean (Gossler
38 and Kind 1996; Deuss and Woodhouse 2001). In particular, seismic studies have found
39 two discontinuities at ~500 km and 560 km depths in some local regions (Deuss and
40 Woodhouse 2001), rather than a single 520-km discontinuity. Therefore, understanding
41 the nature of the wadsleyite-ringwoodite phase transition is of great importance for the
42 interpretation of the 520-km discontinuity.

43 Many experimental studies have investigated the phase boundary between
44 wadsleyite and ringwoodite and found that for the $(\text{Mg}_{0.9}\text{Fe}_{0.1})_2\text{SiO}_4$ system under dry
45 condition, this phase transition occurs at ~520 km along the mantle adiabat, with a
46 Clapeyron slope of ~+4.2 MPa/K (Akaogi et al. 1989; Katsura and Ito 1989; Inoue et
47 al. 2006; Tsujino et al. 2019). The effective width of the two-phase coexistence is 20–
48 22 km, which is much thicker than that of the olivine-wadsleyite binary loop (Inoue et
49 al. 2006; Tsujino et al. 2019). The velocity and density contrasts (ΔV_P , ΔV_S , and $\Delta\rho$)
50 between ringwoodite and wadsleyite are ~3.6%, 4.3%, and 1.9% (Núñez Valdez et al.
51 2012), respectively, smaller than those across the olivine-wadsleyite transition (Núñez-
52 Valdez et al. 2013; Wang et al. 2019). In a pyrolitic composition consisting of ~60%
53 wadsleyite, this phase transition can only result in a ΔV_P of ~2.1%, ΔV_S of 2.6%, and
54 $\Delta\rho$ of 1.1% in a width of 20-22 km, probably making it difficult to be detected as a
55 seismic discontinuity. However, it is not well known why the 520-km discontinuity
56 could be observed in some local regions.

57 One of the most novel features of wadsleyite and ringwoodite is that they can store
58 up to one weight percent of water at MTZ's conditions (Demouchy 2005; Jacobsen et
59 al. 2005; Ohtani 2015; Fei and Katsura 2020), making the MTZ a potential water
60 reservoir in the Earth's interior. Although the actual amount of water constrained from
61 electrical conductivity differ by more than one order of magnitude (Huang et al. 2005;
62 Kelbert et al. 2009; Karato 2011), the discoveries of a hydrous ringwoodite inclusion
63 with ~1.4 wt% water and ice-VII inclusions in natural 'superdeep' diamonds (Pearson
64 et al. 2014; Tschauner et al. 2018) reveal that the MTZ is at least locally hydrated. The
65 presence of water was proposed to narrow the width of the wadsleyite-ringwoodite
66 binary loop (Inoue et al. 2010a), and wadsleyite was found to contain more water than
67 the coexisting ringwoodite with a partition coefficient of 1.6-2.2 at 1673 K (Inoue et al.
68 2010b). However, available data are not sufficient to quantify the water effect on the
69 phase boundary and the water partition coefficient along the mantle geotherm. It is still
70 unknown how water partitioning between wadsleyite and ringwoodite affects the
71 velocity and density jumps across this phase boundary.

72 In this study, we used first-principles calculations to investigate the water effect
73 on the wadsleyite-ringwoodite phase transition and the water partition coefficient
74 across this phase boundary. Combining with high P-T elastic data from previous studies
75 (Núñez Valdez et al. 2012; Núñez-Valdez et al. 2013; Wang et al. 2019), we also
76 estimated the velocity and density jumps caused by the wadsleyite-ringwoodite
77 transition under different conditions. This work provides reliable results to infer the
78 nature of the 520-km discontinuity.

79

80 **2. Methods**

81 **2.1 H₂O partition coefficient**

82 The equilibrium partition coefficient of a dilute component between two pure
83 solids is determined by the Gibbs free energies of their pure and dilute phases.
84 Following the procedures in Hernández et al. (2013) and Townsend et al. (2016), the

85 Gibbs free energy (G) of wadsleyite/ringwoodite with variable water content can be
 86 estimated from the Gibbs free energies of pure wadsleyite/ringwoodite (Mg_2SiO_4) and
 87 the defective cell containing a single defect. Given a collection of N unit cells of
 88 wadsleyite, and n_{Wads} unit cells of wadsleyite which contains a single defect, the
 89 Gibbs free energy of this H_2O -bearing wadsleyite can be written as:

$$90 \quad G_{Wads}(n_{Wads}) = (N - n_{Wads})G_{Wads}^{pure} + n_{Wads}G_{Wads}^{defect} - TS_{Wads}^{conf}(n_{Wads}) \quad (1)$$

91 where G_{Wads}^{pure} and G_{Wads}^{defect} are the Gibbs free energies of pure wadsleyite (Mg_2SiO_4)
 92 and the hydrous wadsleyite with a single defect, respectively. T is temperature, and
 93 S_{Wads}^{conf} is configurational entropy, which can be expressed as:

$$94 \quad S_{Wads}^{conf}(n_{Wads}) = k_B \ln \left(\frac{N_{Wads}!}{(N_{Wads} - n_{Wads})! n_{Wads}!} \right) \quad (2)$$

95 where N_{Wads} is the number of possible crystallographic sites of the defect in
 96 wadsleyite with N unit cells and k_B is the Boltzmann constant. The partial
 97 molar derivative of $G_{Wads}(n_{Wads})$ is:

$$98 \quad \frac{\partial G_{Wads}(n_{Wads})}{\partial n_{Wads}} = -G_{Wads}^{pure} + G_{Wads}^{defect} - T \frac{\partial S_{Wads}^{conf}(n_{Wads})}{\partial n_{Wads}} = G_{Wads}^f - T \frac{\partial S_{Wads}^{conf}(n_{Wads})}{\partial n_{Wads}} \quad (3)$$

$$99 \quad G_{Wads}^f = G_{Wads}^{defect} - G_{Wads}^{pure} \quad (4)$$

100 The partial molar derivative of the configurational entropy is:

$$101 \quad \frac{\partial S_{Wads}^{conf}(n_{Wads})}{\partial n_{Wads}} = k_B \ln \left(\frac{N_{Wads} - n_{Wads}}{n_{Wads}} \right) \quad (5)$$

102 Similarly, the partial molar derivative of the Gibbs free energy of hydrous ringwoodite
 103 can be written as:

$$104 \quad \frac{\partial G_{RW}(n_{RW})}{\partial n_{RW}} = -G_{RW}^{pure} + G_{RW}^{defect} - T \frac{\partial S_{RW}^{conf}(n_{RW})}{\partial n_{RW}} = G_{RW}^f - T \frac{\partial S_{RW}^{conf}(n_{RW})}{\partial n_{RW}} \quad (6)$$

$$105 \quad G_{RW}^f = G_{RW}^{defect} - G_{RW}^{pure} \quad (7)$$

106 where G_{RW}^{pure} and G_{RW}^{defect} are the Gibbs free energies of pure ringwoodite (Mg_2SiO_4)
 107 and the hydrous ringwoodite with a single defect, respectively. $S_{RW}^{conf}(n_{RW})$ is
 108 configurational entropy and n_{RW} is the number of unit cells of ringwoodite that

109 contains a single defect. As such, the partial molar derivative of $S_{RW}^{conf}(n_{RW})$ is:

$$110 \quad \frac{\partial S_{RW}^{conf}(n_{RW})}{\partial n_{RW}} = k_B \ln \left(\frac{N_{RW} - n_{RW}}{n_{RW}} \right) \quad (8)$$

111 where N_{Wads} is the number of possible crystallographic sites of the defect in
 112 ringwoodite. At equilibrium, $\frac{\partial G_{Wads}(n_{Wads})}{\partial n_{Wads}} = \frac{\partial G_{RW}(n_{RW})}{\partial n_{RW}}$, and the H₂O partition
 113 coefficient between wadsleyite and ringwoodite ($D_{H_2O}^{Wads-Rw}$) is the ratio of the number
 114 of defects in wadsleyite and ringwoodite, which can be expressed as:

$$115 \quad D_{H_2O}^{Wads-Rw} = \frac{n_{Wads}}{n_{RW}} = \frac{N_{Wads}}{N_{RW}} \frac{e^{\frac{G_{RW}^f}{k_B T} + 1}}{\frac{G_{Wads}^f}{k_B T} + 1} \approx \frac{N_{Wads}}{N_{RW}} e^{\frac{G_{RW}^f - G_{Wads}^f}{k_B T}} \quad (9)$$

116 2.2 Defect structures of hydrous wadsleyite and ringwoodite

117 The orthorhombic structure of dry wadsleyite with space group *Imma* has three
 118 types of Mg sites [M1(4a), M2(4e) and M3(8g)] and four types of O sites [O1(4e),
 119 O2(4e), O3(8h) and O4(16j)]. The O1 oxygen, which is not bonded to silicon, is an
 120 ideal candidate site for hydroxyls (Smyth 1987). By replacing one M3 Mg atom in the
 121 unit cell of wadsleyite (Mg₁₆Si₈O₃₂) with two H atoms, we constructed the initial
 122 structure of hydrous wadsleyite containing 1.63 wt.% water (Mg₁₅Si₈O₃₀(OH)₂).
 123 According to previous first-principles calculations (Tsuchiya and Tsuchiya 2009; Wang
 124 et al. 2019), the structure with two OH dipoles oriented along the edges of Mg M3 site
 125 is most stable (Fig. 1).

126 Dry ringwoodite (^{IV}A^{VI}B₂O₄) has a normal spinel structure with space group Fd-
 127 3m. In Mg end-member ringwoodite, the four-coordinated A site (8a) is occupied by Si
 128 atom, and the six-coordinated B site (16d) is occupied by Mg atom. Hydrogen was
 129 found to be dissolved into ringwoodite through three candidate mechanisms (Panero
 130 2010): (1) V_{Mg}^{''} + 2H^{**}, Mg vacancy with charge-balanced by two H atoms; (2) V_{Si}^{''''}
 131 + 4H^{****}, Si vacancy with charge-balanced by four H atoms; (3) Mg_{Si}^{''} + 2H^{**}, Si
 132 vacancy is occupied by Mg atom with charge-balanced by two H atoms. Previous first-
 133 principles calculations (Panero 2010; Hernández et al. 2013) found that hydrogen is
 134 mainly incorporated into ringwoodite through the mechanism V_{Mg}^{''} + 2H^{**}, which is

135 also supported by the recent experimental results from nuclear resonance spectroscopy
136 (Grüninger et al. 2017). Thus, we adopted the substitution mechanism $V_{Mg}'' + 2H^{**}$ to
137 construct the initial structure of hydrous ringwoodite with 1.63 wt% water
138 ($Mg_{15}Si_8O_{30}(OH)_2$), where the sites for two H atoms were determined by following the
139 experimental results from pulsed neutron diffraction (Purevjav et al. 2014) (Fig. 1).

140 We did not consider the other two mechanisms because they represent different
141 bulk compositions and hence it is difficult to directly compare their energies with that
142 of wadsleyite, which dissolves water via the mechanism $V_{Mg}'' + 2H^{**}$. Because the
143 other two mechanisms have relatively higher formation enthalpies than the mechanism
144 $V_{Mg}'' + 2H^{**}$ (Panero 2010), it can be inferred that hydrous ringwoodite would have
145 higher energy when all three possible mechanisms are taken into account. Based on the
146 relative defect energies and the ratios between different mechanisms ((1):(2):(3)=
147 65:25:10) calculated in Panero (2010), the energy will increase by 3-5 kJ/mol at 1000-
148 1500 K. Thus, the phase-transition pressure will correspondingly increase by 0.6-1.0
149 GPa and the water partition coefficient between wadsleyite and ringwoodite will
150 increase by 0.2-0.4. It should be noted that these values are only the first-order estimates
151 for the effect of the other two mechanisms.

152 **2.3 First-principles calculations**

153 Calculating the Gibbs free energies of anhydrous and hydrous wadsleyite and
154 ringwoodite is key to obtain the water partition coefficient between these two phases.
155 In theory, the Gibbs free energy G at given pressure P and temperature T is defined by:

$$156 \quad G(P, T) = F(V, T) + PV \quad (10)$$

157 where $F(V, T)$ is the Helmholtz free energy at certain volume V and temperature T .
158 Within the quasi-harmonic approximation (QHA), the F can be expressed in as:

$$159 \quad F(V, T) = U(V) + \frac{1}{2} \sum_{q,m} \hbar \omega_{q,m}(V) + k_B T \sum_{q,m} \ln \left\{ 1 - \exp \left[- \frac{\hbar \omega_{q,m}(V)}{k_B T} \right] \right\} \quad (11)$$

160 In Eq. (11), $q, m, \omega_{q,m}$ are the phonon wave vector, the normal index, and vibrational
161 frequencies of the system respectively; \hbar and k_B refer to the Planck and Boltzmann
162 constants, respectively; the first, second, third terms are the static internal, zero-point,

163 and vibrational energy contributions under temperature T at equilibrium volume V ,
164 respectively.

165 To obtain the static internal energies and vibrational density of states at variable
166 volumes, we performed first-principles calculations using Quantum Espresso package
167 (Giannozzi et al. 2009) based on the density functional theory (DFT), adopting the
168 generalized gradient approximation (GGA) (Perdew et al. 1996) for the exchange-
169 correlation functional. The pseudopotential for magnesium was generated by the von
170 Barth and Car method and pseudopotentials for silicon and oxygen were generated by
171 Troullier-Martins method (Troullier and Martins 1991). More relevant details about the
172 generations for Mg, Si, and O pseudopotentials can be found in Tsuchiya et al. (2004).
173 The pseudopotential for hydrogen is PBE type generated by Troullier-Martins method
174 with the valence configuration of $1s^1$ and the cutoff radius of 1.1 Bohr. Electronic wave
175 functions were expanded by a plane-wave basis with an energy cutoff of 70 Ry. All
176 structures were well optimized at different pressures using the variable cell-shape
177 damped molecular dynamics approach (Wentzcovitch 1991) on a $6\times 6\times 6$ q-point mesh
178 and then their vibrational frequencies were calculated using the ab initio lattice
179 dynamics (LD) (Alfè 2009). Thus, the Helmholtz free energies were calculated from
180 the static energies and vibrational density of states (Eq. (11)) based on the QHA. The
181 calculated Helmholtz free energy versus volume was fitted by the isothermal third-order
182 finite strain equation of state. Thermodynamic properties including pressures at variable
183 volumes and temperatures (equation of state) can be calculated from $F(V, T)$ and the
184 Gibbs free energy can be obtained using Eq. (10). The volume versus pressure
185 relationship is described by the Birch-Murnaghan third-order equation of state.

186

187 **3. Results**

188 **3.1 Relaxed structures of hydrous wadsleyite and ringwoodite**

189 The crystal structures of hydrous wadsleyite and ringwoodite containing 1.63 wt.%
190 H_2O via the substitution mechanism $Mg^{2+} \leftrightarrow 2H^+$ are shown in Fig. 1. The hydrogen

191 bond lengths for all the defect structures ($\text{Mg}_{15}\text{Si}_8\text{O}_{30}(\text{OH})_2$) at different pressures are
192 given in Table 1. At ambient pressure, the calculated H–O bond at static conditions for
193 hydrous wadsleyite is 0.992 Å, close to the experimental data (Purevjav et al. 2016).
194 Over the entire pressure range investigated in this study (0–25 GPa), the H–O bonds
195 for the defect structures of hydrous ringwoodite are relatively longer than those for
196 hydrous wadsleyite. As a consequence, hydrous wadsleyite has a stronger H–O bond
197 and a higher vibrational frequency for the H–O bond compared to hydrous ringwoodite.
198 This can be well explained by the difference in oxygen for H–O bonds. In wadsleyite,
199 H atoms are bonded to the O1 atoms that are not bonded to silicon (Smyth 1987), while
200 all oxygen atoms in ringwoodite are bonded to both Mg and Si atoms. Upon
201 compression from 0 to 20 GPa, the H–O bond in hydrous wadsleyite lengthens by
202 ~1.0%, and in hydrous ringwoodite, the H–O bond lengthens by ~2.7%. As shown in
203 Table 1, the hydrogen bonds in hydrous wadsleyite and ringwoodite are highly
204 asymmetric and non-linear. The hydrogen bond in hydrous ringwoodite is much
205 stronger, with a hydrogen bond length $d(\text{H}\dots\text{O})$ about 18% shorter than in hydrous
206 wadsleyite. Meanwhile, the hydrogen-bonded oxygen distance $d(\text{O}\dots\text{O})$ in hydrous
207 ringwoodite is also about 12% shorter than in hydrous wadsleyite. At 0–20 GPa, both
208 $d(\text{H}\dots\text{O})$ and $d(\text{O}\dots\text{O})$ significantly decrease with pressure, with a decrease of 10–12%
209 in $d(\text{H}\dots\text{O})$ and 5–8% in $d(\text{O}\dots\text{O})$.

210 **3.2 Water effect on wadsleyite-ringwoodite phase transition**

211 The phase boundary between wadsleyite and ringwoodite can be obtained by
212 comparing their Gibbs free energies (Fig. 2). Our calculations show that Mg_2SiO_4
213 undergoes a phase transition from wadsleyite to ringwoodite at 22.7 GPa and 1800 K
214 and the Clapeyron slope is about +3.9 MPa/K (Fig. 3 and 4), consistent with previous
215 GGA calculations (Yu et al. 2008). The transition pressure predicted in this study is
216 about 3 GPa higher than previous experimental measurements (Katsura and Ito 1989;
217 Suzuki et al. 2000; Inoue et al. 2006), but the calculated Clapeyron slope agrees well
218 with experimental results (Fig. 4). Typically, the local density approximation (LDA)

219 underestimates but GGA overestimates the phase-transition pressures for silicate
220 minerals (Yu et al. 2008). Instead, the calculated Clapeyron slope is not essentially
221 sensitive to the exchange-correlation functional used in DFT calculations (Yu et al.
222 2008; Wentzcovitch et al. 2010). We also calculated the phase boundary for the
223 $\text{Mg}_{15}\text{Si}_8\text{O}_{32}\text{H}_2$ system, as shown in Fig. 3 and 4. The incorporation of 2H^+ into the Mg
224 site increases the difference of Gibbs free energy between ringwoodite and wadsleyite
225 nearby the phase-transition pressures, shifting the phase boundary to higher pressures.
226 For instance, at 1500 K, the phase-transition pressure increases from 21.6 GPa in
227 $\text{Mg}_{16}\text{Si}_8\text{O}_{32}$ to 22.8 GPa in $\text{Mg}_{15}\text{Si}_8\text{O}_{32}\text{H}_2$. The pressure shift decreases with increasing
228 temperature because $\text{Mg}_{15}\text{Si}_8\text{O}_{32}\text{H}_2$ ringwoodite has a larger value of configurational
229 entropy than $\text{Mg}_{15}\text{Si}_8\text{O}_{32}\text{H}_2$ wadsleyite. Accordingly, the Clapeyron slope decreases
230 from +3.9 MPa/K in $\text{Mg}_{16}\text{Si}_8\text{O}_{32}$ to +2.5 MPa/K in $\text{Mg}_{15}\text{Si}_8\text{O}_{32}\text{H}_2$. Here we considered
231 the hydrous wadsleyite/ringwoodite as a simple phase with a single component to
232 approximate the water effect on the phase boundary. The presence of water in the
233 $\text{Mg}_{16}\text{Si}_8\text{O}_{32}$ system, more accurately, will result in the coexistence of wadsleyite and
234 ringwoodite at a certain pressure range.

235 In order to determine the two-phase coexistence domain of the $\text{Mg}_2\text{SiO}_4\text{-H}_2\text{O}$
236 system, we calculated the Gibbs free energies of wadsleyite and ringwoodite as a
237 function of water concentration using Eq. (1-2), as shown in Fig. 5. For instance, at
238 1500 K and 20 GPa, the Gibbs free energy of wadsleyite is lower than that of
239 ringwoodite (Fig. 5a), suggesting that wadsleyite is a stable phase under the current
240 conditions. At 24 GPa, the Gibbs free energy of ringwoodite is smaller than that of
241 wadsleyite, indicating the completion of the phase transition. At 22 GPa, these two
242 curves cross over, and the wadsleyite-ringwoodite phase transition occurs. At
243 equilibrium, the chemical potentials of the two phases should be equal. Thus, the water
244 concentrations in wadsleyite and ringwoodite can be derived by calculating the
245 common tangent of two crossed curves. Using this approach, we obtained the
246 dependences of water concentrations in wadsleyite and ringwoodite on pressure at

247 different temperatures (Fig. 5d-5f). The two-phase loop can be determined by searching
248 the two pressures where wadsleyite and ringwoodite have equal water concentrations.
249 Our results show that at the water concentration of 1.0 wt%, wadsleyite and ringwoodite
250 coexist within 0.22 GPa at 1500 K (Fig. 5d), corresponding to 5.5 km. Such a narrow
251 interval will decrease to 0.05 GPa (1.3 km) at 1800 K (Fig. 5e) and less than 0.02 GPa
252 (500 m) at 2000 K (Fig. 5f), suggesting that the presence of water does not significantly
253 change the sharpness of Mg_2SiO_4 wadsleyite-ringwoodite transition. Similarly,
254 previous experimental works also found that the pressure interval is not greater than 0.2
255 GPa in the Mg_2SiO_4 system (Inoue et al. 2010a). By comparison, the pressure interval
256 of two-phase coexistence for the $(\text{Mg}_{0.9}\text{Fe}_{0.1})_2\text{SiO}_4$ system is about 1.0 GPa at 1873 K
257 (Akaogi et al. 1989; Katsura and Ito 1989; Tsujino et al. 2019).

258 Here the Gibbs free energies of wadsleyite and ringwoodite were calculated based
259 on the QHA, which assumes temperature-independent phonon frequencies. With
260 increasing temperature, the anharmonic effect will become significant and may need to
261 be considered. However, the anharmonic contribution declines with increasing pressure,
262 and previous studies have verified the validity of QHA at MTZ conditions (Yu et al.
263 2008; Wentzcovitch et al. 2010). We also did not consider the combined effects of iron
264 and water on the two-phase loop because huge computation is required to quantify the
265 Gibbs free energies of wadsleyite and ringwoodite as a function of iron and water
266 concentrations. The pressure interval for a hydrous and Fe-bearing system can be
267 inferred from the slopes of lower- and upper-boundary pressures on water concentration
268 (k_{wads} and k_{rw}). As shown in Fig. 6, the pressure interval at a water concentration of x
269 will be $\Delta P = (P_{\text{rw}} - P_{\text{wads}}) - x * (k_{\text{wads}} - k_{\text{rw}})$, where $P_{\text{rw}} - P_{\text{wads}}$ is the pressure interval under dry
270 condition. For the $(\text{Mg}_{0.9}\text{Fe}_{0.1})_2\text{SiO}_4$ system with 1.0 w% H_2O , Inoue et al. (2010a)
271 suggested that compared to the anhydrous boundary, the lower and upper boundaries at
272 1673 K shift towards the higher pressure by 0.6-0.8 GPa and ~ 0.2 GPa, respectively,
273 corresponding to a k_{wads} of 0.6-0.8 GPa/wt% and a k_{rw} of 0.2 GPa/wt%. Thus, ΔP for
274 the $(\text{Mg}_{0.9}\text{Fe}_{0.1})_2\text{SiO}_4$ system with 1.0 w% H_2O is 0.2-0.4 GPa (5-10 km). Notably,

275 because the pressure interval for the Fe-bearing system under dry conditions decreases
276 with temperature (Tsuji et al. 2019), ΔP is < 0.24 GPa (6 km) under the representative
277 temperature of mid-MTZ (~ 1800 K), if k_{wad} and k_{rw} at 1673 K are used. Therefore, we
278 conclude that for the $(\text{Mg}_{0.9}\text{Fe}_{0.1})_2\text{SiO}_4$ system, the incorporation of 1.0 wt% water can
279 narrow the effective width of two-phase coexistence by two-thirds.

280 **3.3 H₂O partition coefficient between wadsleyite and ringwoodite**

281 From the Gibbs free energy differences between anhydrous and hydrous phases,
282 we computed the H₂O partition coefficient between wadsleyite and ringwoodite ($D^{\text{Wads-}}$
283 $\text{Rw}_{\text{H}_2\text{O}}$) in Fig. 7. The $D^{\text{Wads-Rw}}_{\text{H}_2\text{O}}$ is larger than one at every P-T point along the phase
284 boundary, indicating that there are more Mg-2H defects in wadsleyite than ringwoodite
285 in thermodynamic equilibrium. Along the phase boundary, the $D^{\text{Wads-Rw}}_{\text{H}_2\text{O}}$ decreases
286 from ~ 3.2 at 1000 K to ~ 1.1 at 2000 K, indicating that more water is preferentially
287 incorporated into wadsleyite relative to the coexisting ringwoodite at equilibration. This
288 is consistent with the stronger H-O bonds in wadsleyite than ringwoodite (Table 1)
289 because the O atoms for H-O bonds in wadsleyite are not bonded to silicon (Fig. 1)
290 (Smyth 1987). Experimental works found that the ratio of H₂O in wadsleyite to
291 coexisting ringwoodite is ~ 1.5 at 1673 K (Chang et al. 2015), consistent with our results
292 (Fig. 7a), although the GGA overestimates the phase boundary by ~ 3 GPa. (Inoue et al.
293 2010b) reported a systematically larger value of 1.6-2.2 for $D^{\text{Wads-Rw}}_{\text{H}_2\text{O}}$ of 1.6-2.2 at
294 1673 K, likely because we did not consider the effect of Si vacancy in hydrous
295 ringwoodite and there may be uncertainties for the measurements of water
296 concentration (Chang et al. 2015). The comparison of $D^{\text{Wads-Rw}}_{\text{H}_2\text{O}}$ between this work
297 and previous experiments of Fe-bearing system indicates that $D^{\text{Wads-Rw}}_{\text{H}_2\text{O}}$ could not be
298 significantly affected by the presence of iron, probably because wadsleyite and
299 ringwoodite have sufficient Mg sites to accommodate both iron and hydrogen atoms
300 even under water-saturated conditions.

301

302 **4. Implication for the 520-km discontinuity**

303 Seismic studies have observed a seismic discontinuity around 520 km depth in
304 some regions such as Northeastern China and central Asia (Shearer 1990; Gossler and
305 Kind 1996; Deuss and Woodhouse 2001; Tian et al. 2016), but it is absent in other
306 regions such as the northeastern Pacific Ocean (Gossler and Kind 1996; Deuss and
307 Woodhouse 2001). Beyond that, instead of one 520-km discontinuity, seismic studies
308 have also found two discontinuities at ~500 km and 560 km depths in some regions
309 (Deuss and Woodhouse 2001), which are ascribed to the wadsleyite-ringwoodite phase
310 transition and the exsolution of Ca-perovskite from garnet (Saikia et al. 2008),
311 respectively.

312 Our results show that the width of the wadsleyite-ringwoodite phase loop in the
313 $\text{Mg}_2\text{SiO}_4\text{-H}_2\text{O}$ system is < 1.3 km at 1800 K, while the incorporation of 1.0 wt% water
314 in the $(\text{Mg}_{0.9}\text{Fe}_{0.1})_2\text{SiO}_4$ system can narrow the effective width of this binary phase loop
315 to ~6 km (Inoue et al. 2010a). Such a depth interval is much thinner than the one under
316 dry conditions (~20 km) and comparable to that of olivine-wadsleyite transition
317 (Katsura et al. 2004). Meanwhile, we also calculated the velocity and density jumps
318 across the wadsleyite-ringwoodite transition under mid-MTZ conditions using the high
319 P-T elastic data from previous studies (Núñez Valdez et al. 2012; Núñez-Valdez et al.
320 2013; Wang et al. 2019, 2020). We consider two end-member cases, the anhydrous
321 system, and wadsleyite with 1.0 wt% H_2O . The water content of ringwoodite is
322 determined by the H_2O partition coefficient (~1.3) in this study. For the
323 $(\text{Mg}_{0.9}\text{Fe}_{0.1})_2\text{SiO}_4$ system, the iron partition coefficient (~0.6) from previous
324 experiments (Inoue et al. 2010a, 2010b) is used to determine the Fe contents in
325 wadsleyite and ringwoodite. Our results show for the $(\text{Mg}_{0.9}\text{Fe}_{0.1})_2\text{SiO}_4$ system, ΔV_P
326 and ΔV_S are ~2.3%, corresponding to V_P and V_S increases of 1.3% in a width of 20 km
327 for a pyrolitic composition. Such small velocity gradients may not be sufficient to
328 produce resolvable seismic signals for a discontinuity at ~520 km. Compared to the
329 anhydrous condition, the presence of 1.0 wt% water will slightly decrease ΔV_P and ΔV_S
330 but increase $\Delta\rho$, which jointly results in a mild increase (~0.2%) in impedance contrasts

331 $(\Delta(\rho V_P)$ and $\Delta(\rho V_S))$ (Table 2). Together with the water effect on the width of the binary
332 phase loop, we conclude that the presence of water in the MTZ will cause much steeper
333 velocity gradients across the wadsleyite-ringwoodite transition, which could promote
334 the occurrence of the 520-km discontinuity. Although this interpretation does not affect
335 the observations using low-frequency seismic methods such as SS precursors and ScS
336 reverberations, the presence of water significantly improves the detectability of the 520-
337 km discontinuity using receiver function methods.

338 Tian et al. (2016) detected a discontinuity around 520 km in the MTZ as well as
339 deeper 410-km and 660-km discontinuities beneath Northeastern China,
340 where the stagnant Pacific slab was also found by tomographic studies (Zhao 2004b,
341 2004a; Zhao and Tian 2013). The presence of water in the regional MTZ likely plays a
342 profound role in the detectability of the 520-km discontinuity. A clear low-velocity
343 anomaly above 410 km in this area also indicates a locally hydrous MTZ (Zhao et al.
344 2009), which may be caused by the water released from the Pacific slab dehydration.
345 Meanwhile, the presence of water in the MTZ can help to explain the depression of the
346 410-km and 660-km discontinuities in this region. Because the Clapeyron slope is
347 positive for the olivine-wadsleyite transition but is negative for the post-spinel
348 transition (Bina and Helffrich 1994; Helffrich and Wood 2001; Higo et al. 2001; Hirose
349 2002; Fei et al. 2004; Katsura et al. 2004), the deeper 410-km and 660-km
350 discontinuities cannot be merely explained by a thermal anomaly. The presence of water
351 will uplift the 410-km discontinuity but deepen the 660-km discontinuity (Higo et al.
352 2001; Chen et al. 2002; Smyth and Frost 2002). As a result, the coupling effect of water
353 and temperature anomaly can provide a good explanation for the simultaneous
354 depression of the 410-km and 660-km discontinuities.

355 The accurate depth of the 520-km discontinuity could vary in a wide depth range
356 because the phase boundary between wadsleyite and ringwoodite is likely affected by
357 multiple factors such as water, temperature, and oxidation conditions (Mrosko et al.
358 2015). For instance, the presence of 1.0 wt% water will deepen the 520-km

359 discontinuity by ~8 km at 1800 K (Fig. 4 and 5), while the lower-temperature anomaly
360 will cause an uplift. The hydration effect on the depth of the 520-km discontinuity is
361 slightly stronger but weaker than these on the 660-km and 410-km discontinuity (Higo
362 et al. 2001; Chen et al. 2002), respectively. However, the 520-km discontinuity is more
363 sensitive to temperature changes than the 410-km and 660-km discontinuities because
364 the Clapeyron slope of the wadsleyite-ringwoodite transition (~+3.9 MPa/K, Fig. 4) is
365 much larger than those of the olivine-wadsleyite and post-spinel transitions (Bina and
366 Helffrich 1994; Helffrich and Wood 2001; Higo et al. 2001; Hirose 2002; Fei et al. 2004;
367 Katsura et al. 2004). This may partly explain the greater depth variation of the 520-km
368 discontinuity than the MTZ bounding discontinuities (Shearer 1990; Gossler and Kind
369 1996; Deuss and Woodhouse 2001; Tian et al. 2016). Further seismic studies on the
370 520-km discontinuity could shed more light on the local hydration and thermal states
371 in the MTZ.

372

373 **5. Conclusion**

374 In this study, we performed first-principles calculations to investigate water
375 partitioning between wadsleyite and ringwoodite and the water effect on the wadsleyite-
376 ringwoodite phase transition. Our results show that upon compression from 0 to 20 GPa,
377 the H–O bond in hydrous wadsleyite lengthens by ~1.0%, and in hydrous ringwoodite,
378 the H–O bond lengthens by ~2.7%. The transition pressure for the Mg₂SiO₄ system
379 predicted in this study is about 3 GPa higher than previous experimental measurements
380 (Katsura and Ito 1989; Suzuki et al. 2000; Inoue et al. 2006), but the calculated
381 Clapeyron slope agrees well with experimental results. The incorporation of 2H⁺ into
382 the Mg site increases the difference of Gibbs free energy between ringwoodite and
383 wadsleyite nearby the phase-transition pressures, shifting the phase boundary to higher
384 pressures. At the water concentration of 1.0 wt%, wadsleyite and ringwoodite coexist
385 within 0.05 GPa (1.3 km) at 1800 K, suggesting that the presence of water does not
386 significantly change the sharpness of Mg₂SiO₄ wadsleyite-ringwoodite transition. For

387 the $(\text{Mg}_{0.9}\text{Fe}_{0.1})_2\text{SiO}_4$ system with 1.0 w% H_2O , the pressure interval is 0.2-0.4 GPa (5-
388 10 km), which is much smaller than that under dry conditions (~ 20 km). Along the
389 phase boundary, the H_2O partition coefficient between wadsleyite and ringwoodite
390 decreases from ~ 3.2 at 1000 K to ~ 1.1 at 2000 K, indicating that more water is
391 preferentially incorporated into wadsleyite relative to the coexisting ringwoodite at
392 equilibration. Combining high P-T elastic data from previous studies and the H_2O
393 partition coefficient in this study, we find that the presence of 1.0 wt% water will
394 slightly decrease ΔV_P and ΔV_S but increase $\Delta \rho$. Given that the incorporation of 1.0 wt%
395 water can narrow the effective width of two-phase coexistence by two-thirds for the
396 $(\text{Mg}_{0.9}\text{Fe}_{0.1})_2\text{SiO}_4$ system, we suggest that the presence of water in the MTZ will cause
397 much steeper velocity gradients across the wadsleyite-ringwoodite transition, which
398 could promote the occurrence of the 520-km discontinuity.

399

400 **Acknowledgments**

401 This study is supported by the Natural Science Foundation of China (41925017,
402 41721002) and the Fundamental Research Funds for the Central Universities
403 (WK2080000144). W.Z. Wang acknowledges support from the UCL-Carnegie
404 Postdoctoral Scholarship. The calculations were conducted partly at the
405 supercomputing center of University of Science and Technology of China.

406 **References**

- 407 Akaogi, M., Ito, E., and Navrotsky, A. (1989) Olivine-modified spinel-spinel
408 transitions in the system Mg_2SiO_4 - Fe_2SiO_4 : Calorimetric measurements,
409 thermochemical calculation, and geophysical application. *Journal of Geophysical*
410 *Research: Solid Earth*, 94, 15671–15685.
- 411 Alfè, D. (2009) PHON: A program to calculate phonons using the small displacement
412 method. *Computer Physics Communications*, 180, 2622–2633.
- 413 Bina, C.R., and Helffrich, G. (1994) Phase transition Clapeyron slopes and transition
414 zone seismic discontinuity topography. *Journal of Geophysical Research*, 99,
415 15853.
- 416 Brown, J.M., and Shankland, T.J. (1981) Thermodynamic parameters in the Earth as
417 determined from seismic profiles. *Geophysical Journal International*, 66, 579–
418 596.
- 419 Chang, Y.Y., Jacobsen, S.D., Bina, C.R., Thomas, S.M., Smyth, J.R., Frost, D.J.,
420 Boffa Ballaran, T., McCammon, C.A., Hauri, E.H., Inoue, T., and others (2015)
421 Comparative compressibility of hydrous wadsleyite and ringwoodite: Effect of
422 H₂O and implications for detecting water in the transition zone. *Journal of*
423 *Geophysical Research B: Solid Earth*, 120, 8259–8280.
- 424 Chen, J., Inoue, T., Yurimoto, H., and Weidner, D.J. (2002) Effect of water on
425 olivine-wadsleyite phase boundary in the $(Mg, Fe)_2SiO_4$ system. *Geophysical*
426 *Research Letters*, 29, 22-1-22–4.
- 427 Demouchy, S. (2005) Pressure and temperature-dependence of water solubility in Fe-
428 free wadsleyite. *American Mineralogist*, 90, 1084–1091.
- 429 Deuss, A., and Woodhouse, J. (2001) Seismic Observations of Splitting of the Mid-
430 Transition Zone Discontinuity in Earth's Mantle. *Science*, 294, 354–357.
- 431 Duan, L., Wang, W., Wu, Z., and Qian, W. (2019) Thermodynamic and Elastic
432 Properties of Grossular at High Pressures and High Temperatures: A First-
433 Principles Study. *Journal of Geophysical Research: Solid Earth*, 124,
434 2019JB017439.
- 435 Dziewonski, A.M., and Anderson, D.L. (1981) Preliminary reference Earth model.
436 *Physics of the Earth and Planetary Interiors*, 25, 297–356.
- 437 Fei, H., and Katsura, T. (2020) High water solubility of ringwoodite at mantle
438 transition zone temperature. *Earth and Planetary Science Letters*, 531, 115987.
- 439 Fei, Y., Van Orman, J., Li, J., van Westrenen, W., Sanloup, C., Minarik, W., Hirose,
440 K., Komabayashi, T., Walter, M., and Funakoshi, K. (2004) Experimentally
441 determined postspinel transformation boundary in Mg_2SiO_4 using MgO as an
442 internal pressure standard and its geophysical implications. *Journal of*
443 *Geophysical Research: Solid Earth*, 109, 1–8.
- 444 Giannozzi, P., Baroni, S., Bonini, N., Calandra, M., Car, R., Cavazzoni, C., Ceresoli,
445 D., Chiarotti, G.L., Cococcioni, M., Dabo, I., and others (2009) QUANTUM
446 ESPRESSO: a modular and open-source software project for quantum
447 simulations of materials. *Journal of Physics: Condensed Matter*, 21, 395502.

- 448 Gossler, J., and Kind, R. (1996) Seismic evidence for very deep roots of continents.
449 Earth and Planetary Science Letters, 138, 1–13.
- 450 Grüniger, H., Armstrong, K., Greim, D., Boffa-Ballaran, T., Frost, D.J., and Senker,
451 J. (2017) Hidden Oceans? Unraveling the Structure of Hydrous Defects in the
452 Earth's Deep Interior. Journal of the American Chemical Society, 139, 10499–
453 10505.
- 454 Helffrich, G.R., and Wood, B.J. (2001) The Earth's mantle. Nature, 412, 501–507.
- 455 Hernández, E.R., Alfè, D., and Brodholt, J. (2013) The incorporation of water into
456 lower-mantle perovskites: A first-principles study. Earth and Planetary Science
457 Letters, 364, 37–43.
- 458 Higo, Y., Inoue, T., Irifune, T., and Yurimoto, H. (2001) Effect of water on the spinel-
459 postspinel transformation in Mg_2SiO_4 . Geophysical Research Letters, 28, 3505–
460 3508.
- 461 Hirose, K. (2002) Phase transitions in pyrolitic mantle around 670-km depth:
462 Implications for upwelling of plumes from the lower mantle. Journal of
463 Geophysical Research: Solid Earth, 107, ECV 3-1-ECV 3-13.
- 464 Huang, X., Xu, Y., and Karato, S. (2005) Water content in the transition zone from
465 electrical conductivity of wadsleyite and ringwoodite. Nature, 434, 746–749.
- 466 Inoue, T., Irifune, T., Higo, Y., Sanehira, T., Sueda, Y., Yamada, A., Shinmei, T.,
467 Yamazaki, D., Ando, J., Funakoshi, K., and others (2006) The phase boundary
468 between wadsleyite and ringwoodite in Mg_2SiO_4 determined by in situ X-ray
469 diffraction. Physics and Chemistry of Minerals, 33, 106–114.
- 470 Inoue, T., Ueda, T., Tanimoto, Y., Yamada, A., and Irifune, T. (2010a) The effect of
471 water on the high-pressure phase boundaries in the system Mg_2SiO_4 - Fe_2SiO_4 .
472 Journal of Physics: Conference Series, 215, 012101.
- 473 Inoue, T., Wada, T., Sasaki, R., and Yurimoto, H. (2010b) Water partitioning in the
474 Earth's mantle. Physics of the Earth and Planetary Interiors, 183, 245–251.
- 475 Jacobsen, S.D., Demouchy, S., Frost, D.J., Ballaran, T.B., and Kung, J. (2005) A
476 systematic study of OH in hydrous wadsleyite from polarized FTIR spectroscopy
477 and single-crystal X-ray diffraction: Oxygen sites for hydrogen storage in Earth's
478 interior. American Mineralogist, 90, 61–70.
- 479 Karato, S. (2011) Water distribution across the mantle transition zone and its
480 implications for global material circulation. Earth and Planetary Science Letters,
481 301, 413–423.
- 482 Katsura, T., and Ito, E. (1989) The system Mg_2SiO_4 - Fe_2SiO_4 at high pressures and
483 temperatures: Precise determination of stabilities of olivine, modified spinel, and
484 spinel. Journal of Geophysical Research: Solid Earth, 94, 15663–15670.
- 485 Katsura, T., Yamada, H., Nishikawa, O., Song, M., Kubo, A., Shinmei, T., Yokoshi,
486 S., Aizawa, Y., Yoshino, T., Walter, M.J., and others (2004) Olivine-wadsleyite
487 transition in the system $(Mg, Fe)_2SiO_4$. Journal of Geophysical Research: Solid
488 Earth, 109, n/a–n/a.
- 489 Kelbert, A., Schultz, A., and Egbert, G. (2009) Global electromagnetic induction

- 490 constraints on transition-zone water content variations. *Nature*, 460, 1003–1006.
- 491 Kennett, B.L.N., Engdahl, E.R., and Buland, R. (1995) Constraints on seismic
492 velocities in the Earth from traveltimes. *Geophysical Journal International*, 122,
493 108–124.
- 494 Mrosko, M., Koch-Müller, M., McCammon, C., Rhede, D., Smyth, J.R., and Wirth,
495 R. (2015) Water, iron, redox environment: effects on the wadsleyite–ringwoodite
496 phase transition. *Contributions to Mineralogy and Petrology*, 170, 9.
- 497 Núñez-Valdez, M., Wu, Z., Yu, Y.G., and Wentzcovitch, R.M. (2013) Thermal
498 elasticity of $(\text{Fe}_x, \text{Mg}_{1-x})_2\text{SiO}_4$ olivine and wadsleyite. *Geophysical Research*
499 *Letters*, 40, 290–294.
- 500 Núñez Valdez, M., Wu, Z., Yu, Y.G., Revenaugh, J., and Wentzcovitch, R.M. (2012)
501 Thermoelastic properties of ringwoodite $(\text{Fe}_x, \text{Mg}_{1-x})_2\text{SiO}_4$: Its relationship to the
502 520 km seismic discontinuity. *Earth and Planetary Science Letters*, 351–352,
503 115–122.
- 504 Ohtani, E. (2015) Hydrous minerals and the storage of water in the deep mantle.
505 *Chemical Geology*, 418, 6–15.
- 506 Panero, W.R. (2010) First principles determination of the structure and elasticity of
507 hydrous ringwoodite. *Journal of Geophysical Research*, 115, B03203.
- 508 Pearson, D.G., Brenker, F.E., Nestola, F., McNeill, J., Nasdala, L., Hutchison, M.T.,
509 Matveev, S., Mather, K., Silversmit, G., Schmitz, S., and others (2014) Hydrous
510 mantle transition zone indicated by ringwoodite included within diamond.
511 *Nature*, 507, 221–224.
- 512 Perdew, J.P., Burke, K., and Ernzerhof, M. (1996) Generalized Gradient
513 Approximation Made Simple. *Physical Review Letters*, 77, 3865–3868.
- 514 Purevjav, N., Okuchi, T., Tomioka, N., Abe, J., and Harjo, S. (2014) Hydrogen site
515 analysis of hydrous ringwoodite in mantle transition zone by pulsed neutron
516 diffraction. *Geophysical Research Letters*, 41, 6718–6724.
- 517 Purevjav, N., Okuchi, T., Tomioka, N., Wang, X., and Hoffmann, C. (2016)
518 Quantitative analysis of hydrogen sites and occupancy in deep mantle hydrous
519 wadsleyite using single crystal neutron diffraction. *Scientific Reports*, 6, 34988.
- 520 Ringwood, A.E. (1962) A model for the upper mantle. *Journal of Geophysical*
521 *Research*, 67, 857–867.
- 522 Saikia, A., Frost, D.J., and Rubie, D.C. (2008) Splitting of the 520-Kilometer Seismic
523 Discontinuity and Chemical Heterogeneity in the Mantle. *Science*, 319, 1515–
524 1518.
- 525 Shearer, P.M. (1990) Seismic imaging of upper-mantle structure with new evidence
526 for a 520-km discontinuity. *Nature*, 344, 121–126.
- 527 Shearer, P.M., and Flanagan, M.P. (1999) Seismic Velocity and Density Jumps
528 Across the 410- and 660-Kilometer Discontinuities. *Science*, 285, 1545–1548.
- 529 Smyth, J.R. (1987) The beta- Mg_2SiO_4 : a potential host for water in the mantle?
530 *American Mineralogist*, 72, 1051–1055.
- 531 Smyth, J.R., and Frost, D.J. (2002) The effect of water on the 410-km discontinuity:

- 532 An experimental study. *Geophysical Research Letters*, 29, 4.
533 Suzuki, A., Ohtani, E., Morishima, H., Kubo, T., Kanbe, Y., Kondo, T., Okada, T.,
534 Terasaki, H., Kato, T., and Kikegawa, T. (2000) In situ determination of the
535 phase boundary between Wadsleyite and Ringwoodite in Mg_2SiO_4 . *Geophysical*
536 *Research Letters*, 27, 803–806.
- 537 Tian, Y., Zhu, H., Zhao, D., Liu, C., Feng, X., Liu, T., and Ma, J. (2016) Mantle
538 transition zone structure beneath the Changbai volcano: Insight into deep slab
539 dehydration and hot upwelling near the 410 km discontinuity. *Journal of*
540 *Geophysical Research: Solid Earth*, 121, 5794–5808.
- 541 Townsend, J.P., Tsuchiya, J., Bina, C.R., and Jacobsen, S.D. (2016) Water
542 partitioning between bridgmanite and postperovskite in the lowermost mantle.
543 *Earth and Planetary Science Letters*, 454, 20–27.
- 544 Troullier, N., and Martins, J.L. (1991) Efficient pseudopotentials for plane-wave
545 calculations. II. Operators for fast iterative diagonalization. *Physical Review B*,
546 43, 8861–8869.
- 547 Tschauner, O., Huang, S., Greenberg, E., Prakapenka, V.B., Ma, C., Rossman, G.R.,
548 Shen, A.H., Zhang, D., Newville, M., Lanzirotti, A., and others (2018) Ice-VII
549 inclusions in diamonds: Evidence for aqueous fluid in Earth’s deep mantle.
550 *Science*, 359, 1136–1139.
- 551 Tsuchiya, J., and Tsuchiya, T. (2009) First principles investigation of the structural
552 and elastic properties of hydrous wadsleyite under pressure. *Journal of*
553 *Geophysical Research*, 114, B02206.
- 554 Tsuchiya, T., Tsuchiya, J., Umemoto, K., and Wentzcovitch, R.M. (2004) Phase
555 transition in $MgSiO_3$ perovskite in the earth’s lower mantle. *Earth and Planetary*
556 *Science Letters*, 224, 241–248.
- 557 Tsujino, N., Yoshino, T., Yamazaki, D., Sakurai, M., Sun, W., Xu, F., Tange, Y., and
558 Higo, Y. (2019) Phase transition of wadsleyite-ringwoodite in the Mg_2SiO_4 -
559 Fe_2SiO_4 system. *American Mineralogist*, 104, 588–594.
- 560 Wang, W., Walter, M.J., Peng, Y., Redfern, S., and Wu, Z. (2019) Constraining
561 olivine abundance and water content of the mantle at the 410-km discontinuity
562 from the elasticity of olivine and wadsleyite. *Earth and Planetary Science*
563 *Letters*, 519, 1–11.
- 564 Wang, W., Zhang, H., Brodholt, J.P., and Wu, Z. (2020) Elasticity of hydrous
565 ringwoodite at mantle conditions: Implication for water distribution in the
566 lowermost mantle transition zone. *Earth and Planetary Science Letters*, 554,
567 116626.
- 568 Wentzcovitch, R.M. (1991) Invariant molecular-dynamics approach to structural
569 phase transitions. *Physical Review B*, 44, 2358–2361.
- 570 Wentzcovitch, R.M., Yu, Y.G., and Wu, Z. (2010) Thermodynamic Properties and
571 Phase Relations in Mantle Minerals Investigated by First Principles
572 Quasiharmonic Theory. *Reviews in Mineralogy and Geochemistry*, 71, 59–98.
- 573 Yu, Y.G., Wu, Z., and Wentzcovitch, R.M. (2008) α - β - γ transformations in Mg_2SiO_4

- 574 in Earth's transition zone. *Earth and Planetary Science Letters*, 273, 115–122.
- 575 Zhao, D. (2004a) Global tomographic images of mantle plumes and subducting slabs:
576 insight into deep Earth dynamics. *Physics of the Earth and Planetary Interiors*,
577 146, 3–34.
- 578 Zhao, D. (2004b) Origin of the Changbai intraplate volcanism in Northeast China:
579 Evidence from seismic tomography. *Chinese Science Bulletin*, 49, 1401.
- 580 Zhao, D., and Tian, Y. (2013) Changbai intraplate volcanism and deep earthquakes in
581 East Asia: a possible link? *Geophysical Journal International*, 195, 706–724.
- 582 Zhao, D., Tian, Y., Lei, J., Liu, L., and Zheng, S. (2009) Seismic image and origin of
583 the Changbai intraplate volcano in East Asia: Role of big mantle wedge above
584 the stagnant Pacific slab. *Physics of the Earth and Planetary Interiors*, 173, 197–
585 206.
- 586 Zou, F., Wu, Z., Wang, W., and Wentzcovitch, R.M. (2018) An Extended
587 Semianalytical Approach for Thermoelasticity of Monoclinic Crystals:
588 Application to Diopside. *Journal of Geophysical Research: Solid Earth*, 123,
589 7629–7643.
- 590

Table 1. Hydrogen bond geometries at static conditions for hydrous wadsleyite and ringwoodite ($\text{Mg}_{15}\text{Si}_8\text{O}_{30}(\text{OH})_2$) calculated in this study.

Minerals	Pressure (GPa)	d(H-O) (Å)	frequency (cm^{-1})	d(H...O) (Å)	d(O...O) (Å)	
Hydrous wadsleyite	0	0.992	3286	2.014	2.998	This study
	0	1.00	-	-	3.01	ref. 1*
	0	0.999	-	2.089	-	ref. 2†
	0	0.987	-	2.105	-	ref. 2‡
	5	0.995	3227	1.935	2.921	This study
	10	0.997	3172	1.869	2.856	This study
	15	1.000	3121	1.812	2.802	This study
	20	1.002	3072	1.764	2.756	This study
Hydrous ringwoodite	25	1.004	3022	1.723	2.716	This study
	0	1.025	2748	1.668	2.653	This study
	5	1.031	2638	1.620	2.612	This study
	10	1.038	2529	1.576	2.577	This study
	15	1.045	2422	1.539	2.547	This study
	20	1.053	2306	1.500	2.518	This study
25	1.062	2193	1.465	2.492	This study	

ref. 1, Tsuchiya and Tsuchiya (2009); ref. 2, Purevjav et al. (2016). *, static conditions; †, 100 K; ‡, 295 K.

Table 2. Predicted velocity and density contrasts between ringwoodite and wadsleyite at 18 GPa and 1800 K.

Systems	Mg ₂ SiO ₄	Mg ₂ SiO ₄ +1.0 wt% H ₂ O	(Mg _{0.9} Fe _{0.1}) ₂ SiO ₄	(Mg _{0.9} Fe _{0.1}) ₂ SiO ₄ +1.0 wt% H ₂ O
Width of binary phase loop (km)	-	~1.3	~20	~6
ΔK_S	7.70%	7.50%	8.45%	8.28%
ΔG	9.04%	8.77%	8.31%	7.99%
$\Delta \rho$	1.96%	2.67%	3.85%	4.54%
ΔV_P	3.15%	2.68%	2.28%	1.81%
ΔV_S	3.54%	3.05%	2.23%	1.72%
$\Delta(\rho V_P)$	5.11%	5.35%	6.12%	6.36%
$\Delta(\rho V_S)$	5.51%	5.72%	6.08%	6.27%

Elasticity of wadsleyite and ringwoodite is available in previous studies (Núñez Valdez et al. 2012; Núñez-Valdez et al. 2013; Wang et al. 2019). The water partition coefficient (~1.3) in this study and the iron partition coefficient (~0.6) from previous experiments is used.

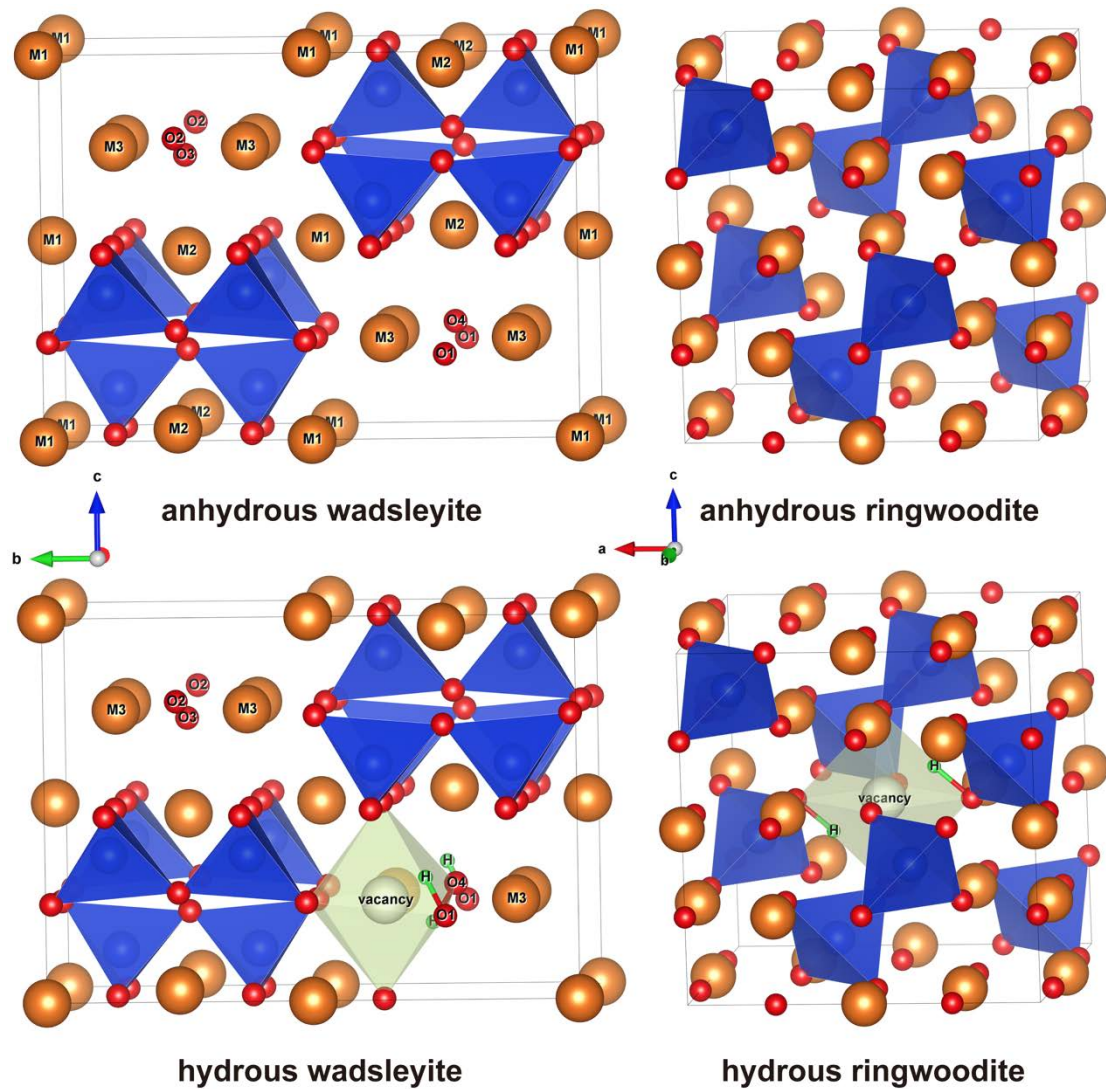


Figure 1. Relaxed crystal structures of anhydrous and hydrous wadsleyite and ringwoodite. In all structures, orange, red, dark blue, and green spheres represent magnesium, oxygen, silicon, and hydrogen atoms, respectively.

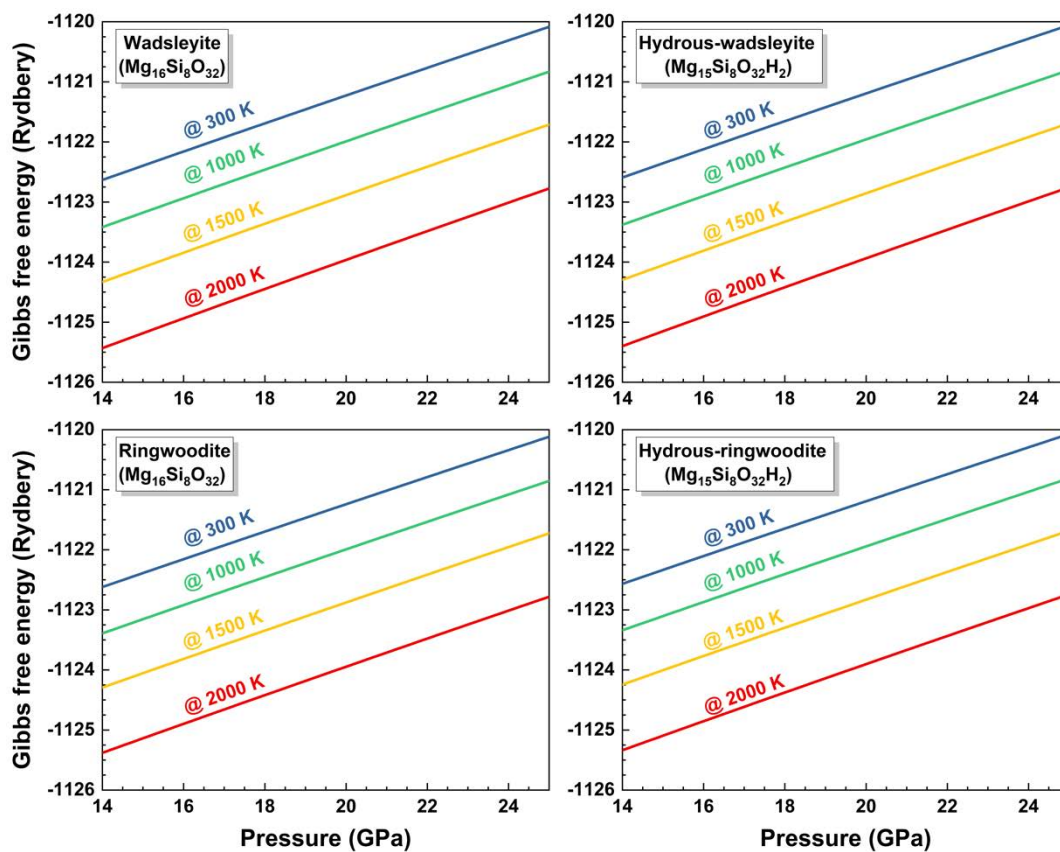


Figure 2. Gibbs free energy of anhydrous and hydrous wadsleyite and ringwoodite ($Mg_{16}Si_8O_{32}$ and $Mg_{15}Si_8O_{32}H_2$) as a function of pressure at various temperatures. The Gibbs free energies of hydrous phases ($Mg_{15}Si_8O_{32}H_2$) do not include the contribution of the configurational entropy.

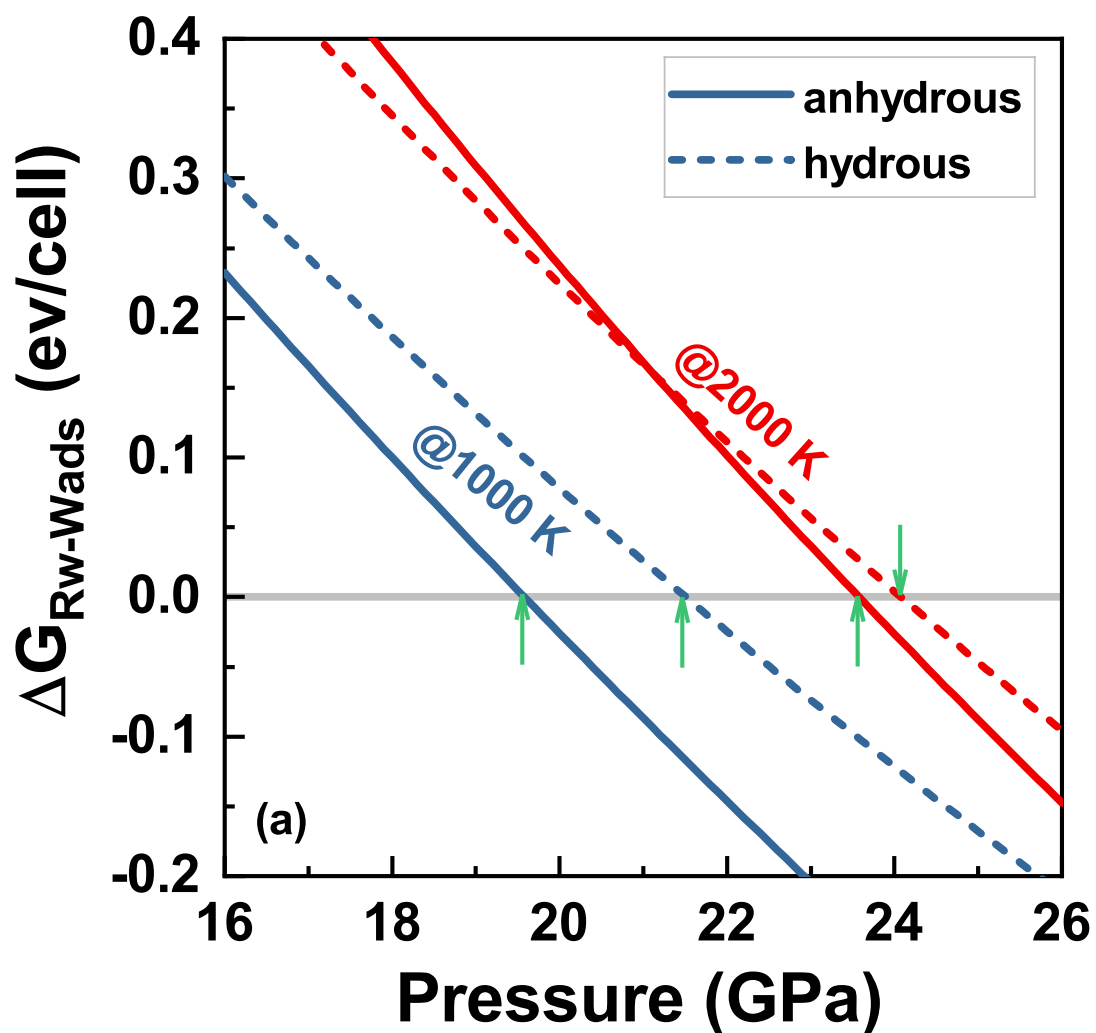


Figure 3. The differences of Gibbs free energy between ringwoodite and wadsleyite. Solid and dash lines represent the G differences between wadsleyite and ringwoodite for Mg₁₆Si₈O₃₂ and Mg₁₅Si₈O₃₂H₂ systems, respectively. The configurational entropies (Eq. (2)) in hydrous wadsleyite and ringwoodite are included to calculate the ΔG .

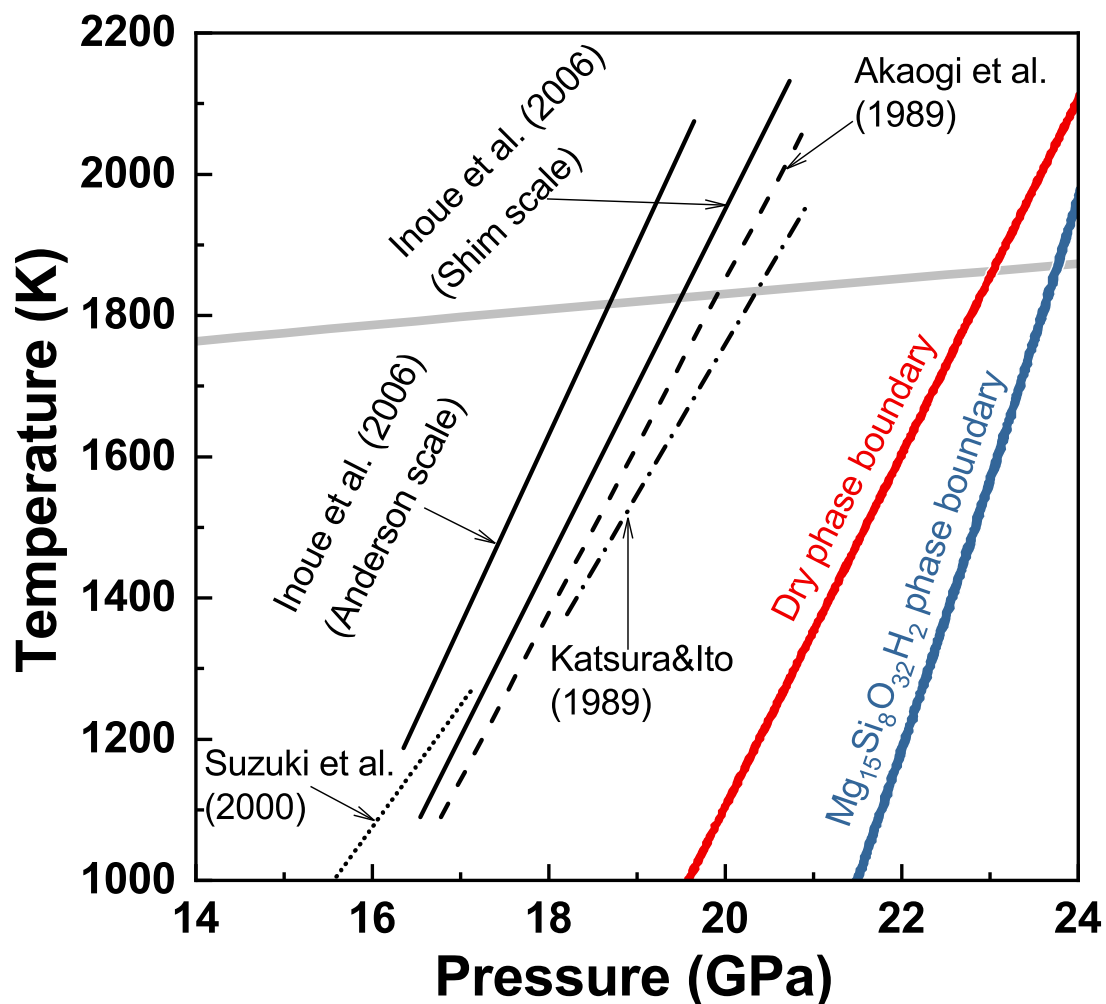


Figure 4. Phase boundary between wadsleyite and ringwoodite. Red and blue lines represent the phase boundaries for $\text{Mg}_{16}\text{Si}_8\text{O}_{32}$ and $\text{Mg}_{15}\text{Si}_8\text{O}_{32}\text{H}_2$ systems, respectively. Experimental results: black lines, (Inoue et al. 2006); dash line, Akaogi et al (1989); short dash line, Suzuki et al. (2000); dash dot line, Katsura and Ito (1989). The grey line is the mantle adiabat Brown and Shankland (1981).

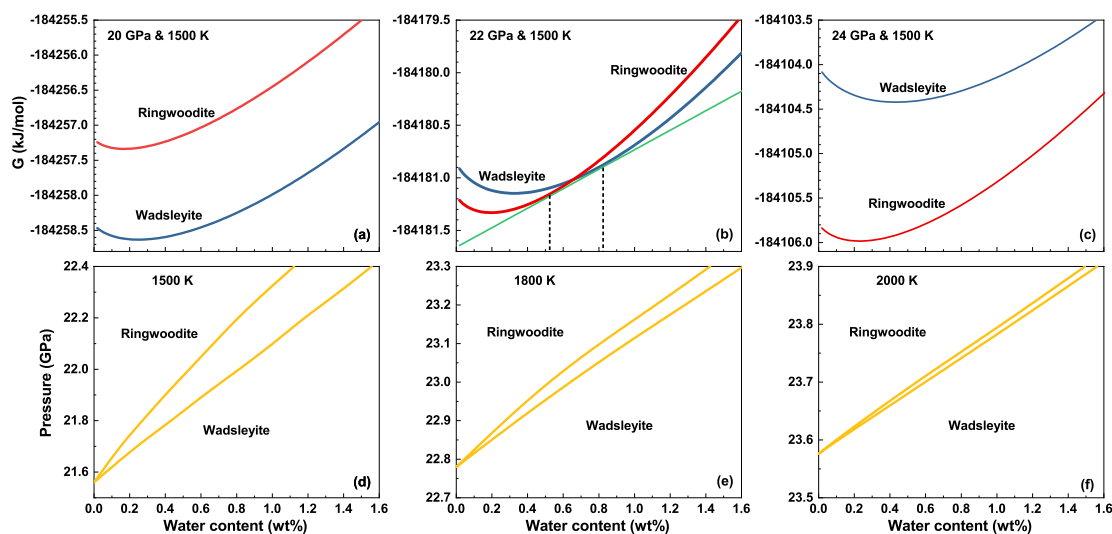


Figure 5. Top: the Gibbs free energies of wadsleyite and ringwoodite versus water concentration at 1500 K and (a) 20 GPa, (b) 22 GPa, (c) 24 GPa. Red and blue lines represent the Gibbs free energies of wadsleyite and ringwoodite, respectively. The green line in (b) is the cotangent line of two crossed curves. Bottom: water effect on the phase loop of wadsleyite-ringwoodite transition in the $\text{Mg}_2\text{SiO}_4\text{-H}_2\text{O}$ system at (d) 1500 K, (e) 1800 K, (f) 2000 K. Wadsleyite and ringwoodite coexist within 0.05 GPa or 1.3 km at 1800 K when the water concentration is 1.0 wt%.

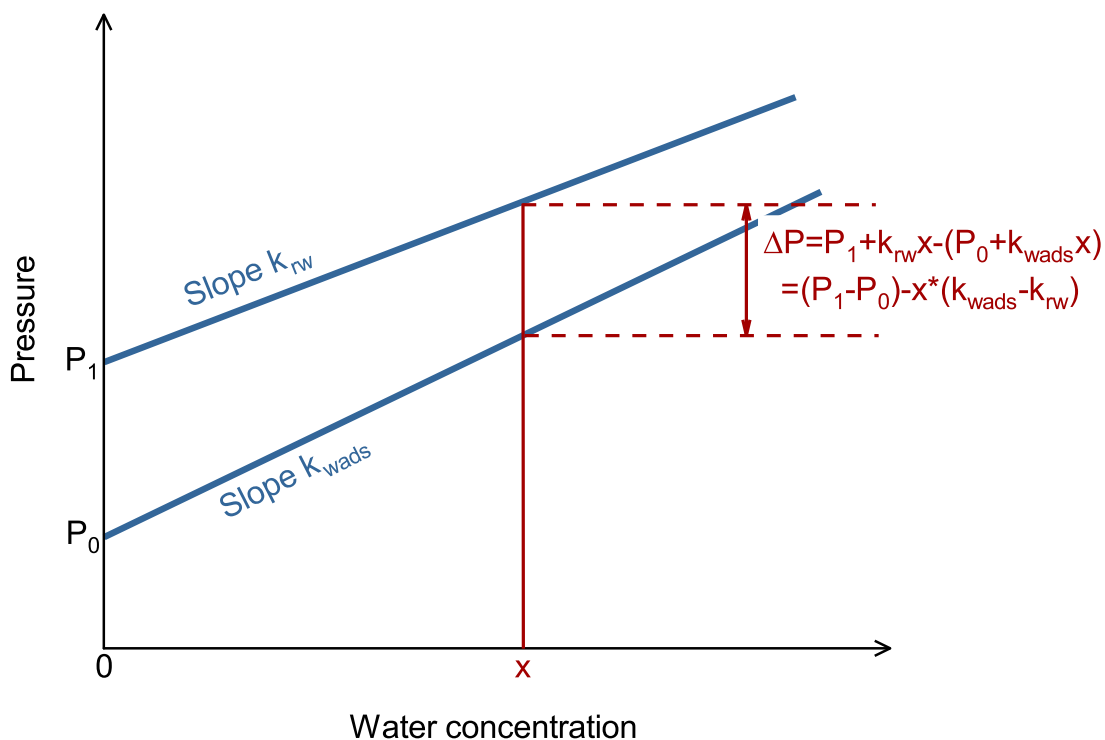


Figure 6. Schematic diagrams of the relationship between the pressure interval of two-phase coexistence for the $(\text{Mg}_{0.9}\text{Fe}_{0.1})_2\text{SiO}_4\text{-H}_2\text{O}$ system. The pressure interval at a water concentration of x is $\Delta P = (D^{\text{Wads-Rw}}_{\text{H}_2\text{O}} - 1) * k_{\text{wads}} * x$. In the $(\text{Mg}_{0.9}\text{Fe}_{0.1})_2\text{SiO}_4\text{-H}_2\text{O}$ system, the pressure interval is $\Delta P = (P_{\text{rw}} - P_{\text{wads}}) - x * (k_{\text{wads}} - k_{\text{rw}})$, where is $P_{\text{rw}} - P_{\text{wads}}$ the pressure interval for the $(\text{Mg}_{0.9}\text{Fe}_{0.1})_2\text{SiO}_4$ system under dry condition. For the $(\text{Mg}_{0.9}\text{Fe}_{0.1})_2\text{SiO}_4$ system with 1.0 wt% H_2O , Inoue et al. (2010a) suggested that compared to the anhydrous boundary, the lower and upper boundaries at 1673 K shift towards the higher pressure by 0.6-0.8 GPa and ~ 0.2 GPa, respectively, corresponding to a k_{wads} of 0.6-0.8 GPa/wt% and a k_{rw} of 0.2 GPa/wt%.

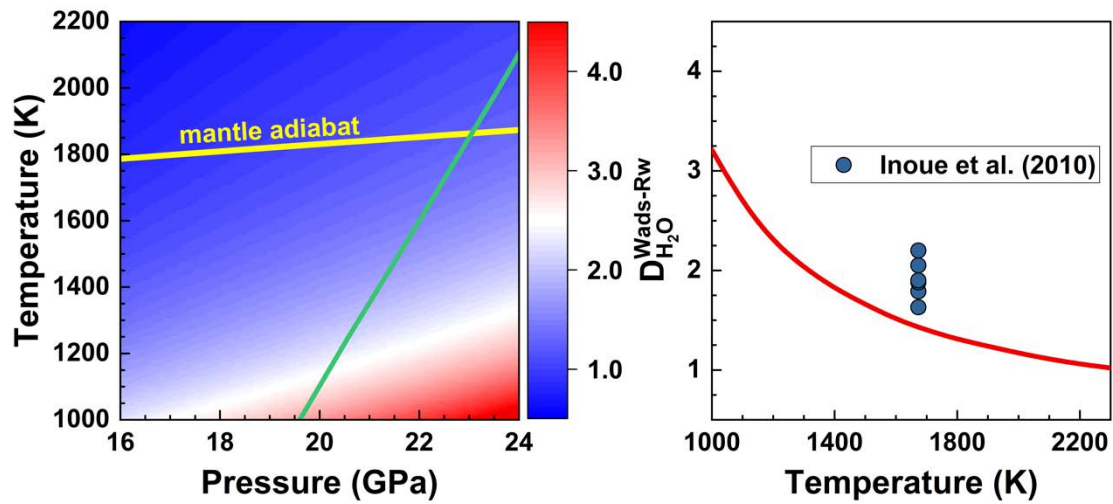


Figure 7. (a) Map of the water partition coefficient between wadsleyite and ringwoodite. The yellow line is the mantle adiabat Brown and Shankland (1981). (b) water partition coefficient along the phase boundary. Experimental results are from Inoue et al. (2010b).